Seasonal cycle of idealized polar clouds: large eddy simulations driven by a GCM

Xiyue Zhang[1], Tapio Schneider[2,3], Zhaoyi Shen[2], Kyle G. Pressel[4], and Ian Eisenman[5]

[1]Johns Hopkins University, Baltimore, Maryland, USA
[2]California Institute of Technology, Pasadena, California, USA
[3]Jet Propulsion Laboratory, California Institute of Technology, Pasadena, California, USA
[4]Pacific Northwest National Laboratory, Richland, Washington, USA
[5]Scripps Institution of Oceanography, University of California, San Diego, California, USA

Key Points:

- LES driven by time-varying large-scale forcings from an idealized GCM is used to simulate the seasonal cycle of Arctic clouds
- Simulated low-level cloud liquid is maximal in late summer to early autumn, and minimal in winter, consistent with observations
- Large-scale advection provides the main moisture source for cloud liquid and shapes its seasonal cycle

Corresponding author: X. Zhang, `sallyz@jhu.edu`

Abstract

The uncertainty in polar cloud feedbacks calls for process understanding of the cloud response to climate warming. As an initial step toward improved process understanding, we investigate the seasonal cycle of polar clouds in the current climate by adopting a novel modeling framework using large eddy simulations (LES), which explicitly resolve cloud dynamics. Resolved horizontal and vertical advection of heat and moisture from an idealized general circulation model (GCM) are prescribed as forcing in the LES. The LES are also forced with prescribed sea ice thickness, but surface temperature, atmospheric temperature, and moisture evolve freely without nudging. A semigray radiative transfer scheme without water vapor and cloud feedbacks allows the GCM and LES to achieve closed energy budgets more easily than would be possible with more complex schemes. This enables the mean states in the two models to be consistently compared, without the added complications from interaction with more comprehensive radiation. We show that the LES closely follow the GCM seasonal cycle, and the seasonal cycle of low-level clouds in the LES resembles observations: maximum cloud liquid occurs in late summer and early autumn, and winter clouds are dominated by ice in the upper troposphere. Large-scale advection of moisture provides the main source of water vapor for the liquid-containing clouds in summer, while a temperature advection peak in winter makes the atmosphere relatively dry and reduces cloud condensate. The framework we develop and employ can be used broadly for studying cloud processes and the response of polar clouds to climate warming.

Plain Language Summary

The polar regions are changing rapidly. Clouds and their feedbacks remain uncertain due to small-scale unresolved processes in climate models, which contribute to uncertainties in polar climate projection. In order to understand the mechanisms that control polar clouds, we focus on their seasonal cycle in the current climate. We adopt an idealized framework for driving high-resolution simulations by a global climate model. With minimal components represented, we find similar features between the simulated and observed polar clouds. In particular, liquid-containing clouds reach maximum in summer, which coincides with the summer peak in moisture advection from lower latitudes. Therefore, projection of polar clouds will depend on future changes in heat and moisture advection. This framework will allow us to study the response of polar clouds to climate warming.

1 Introduction

Clouds in the Arctic display a prominent seasonal cycle in their amount and vertical distribution (Cesana et al., 2012). In particular, the low-level liquid-containing clouds dominate the cloud radiative effect (CRE) on the surface energy budget in all seasons (Persson, 2002; Shupe & Intrieri, 2004). Clouds interact with sea ice on seasonal time scales. For example, springtime Arctic clouds play an important role in determining sea ice extent in autumn (Cox et al., 2016). By examining the cause of the seasonal cycle of polar clouds, we can gain a better understanding of the factors that control the cloud amount and CRE. This is an essential step towards understanding how clouds respond and contribute to climate change in the Arctic (Kay et al., 2016).

Early studies have laid the groundwork for characterizing Arctic clouds and their seasonal cycle (Curry & Herman, 1985; Curry et al., 1996). In particular, Beesley and Moritz (1999) attempted to explain the seasonal variability of Arctic low-level clouds using a single-column model. Large-scale forcing based on reanalysis for summer and winter produced a cloudy summer and a clear winter boundary layer (BL), consistent with observations. They also found that artificially shutting off surface evaporation in summer does not eliminate low-level clouds. This suggests an important role large-scale forcing plays in providing moisture and shaping the seasonal cycle of Arctic clouds.

Advances in active satellite observations over the past decade have provided unprecedented 3D coverage of clouds in polar regions. Total cloud fraction peaks in autumn over the Arctic Ocean, slightly later than what surface-based and passive satellite observations suggested previously (Liu et al., 2012; Kay & L'Ecuyer, 2013). Liquid-containing clouds persist throughout the year over the Arctic Ocean, and the low-level liquid-containing cloud fraction is highest in late summer and autumn. Ice-dominated clouds, on the other hand, show maximum cloud fraction in the winter upper troposphere (Cesana et al., 2012). Consistently, liquid water path (LWP) reaches its maximum in July–September and minimum in winter (Zuidema & Joyce, 2008; Lenaerts et al., 2017). However, it remains challenging for general circulation models (GCMs) to correctly simulate the observed seasonal cycle of Arctic clouds (Karlsson & Svensson, 2013; Taylor et al., 2019; Kretzschmar et al., 2019; Lenaerts et al., 2017) and the cloudy state in winter (Pithan et al., 2014, 2016).

Here we adopt a novel framework by Shen et al. (2020) in which high-resolution models are driven with large-scale fields from a GCM to simulate and analyze the seasonal cycle of polar clouds. It is a modification of the traditional concept of driving limited-domain models with large-scale forcing from observations or global models (Randall & Cripe, 1999; Dal Gesso & Neggers, 2018). Instead of testing cloud and turbulence parameterizations (Krueger, 1988; Betts & Miller, 1986; Neggers et al., 2012), we aim to explain the observed seasonal cycle of Arctic clouds. We use large eddy simulations (LES) to explicitly resolve essential dynamics of clouds and turbulence in the polar troposphere. Although LES have been frequently used to study the Arctic BL (Klein et al., 2009; H. Morrison et al., 2011; Ovchinnikov et al., 2014; Savre et al., 2015), they have rarely been used to simulate the entire Arctic troposphere. The challenge is that LES alone cannot support large-scale circulations because of their limited domain size. GCM outputs can provide large-scale forcing necessary to drive LES. Two advantages are evident: 1) the results are independent on cloud and turbulence parameterizations; 2) the cloud interactions with the large-scale circulation are absent. Understanding how large-scale circulation drives cloud variability is a necessary step toward disentangling complex cloud feedback processes.

As a first step, we choose an idealized framework that captures components crucial to Arctic clouds, such as large-scale advection, a closed surface energy budget with sea ice, and mixed-phase microphysics. Following Shen et al. (2020), we use a GCM with simple radiation and convection schemes but without clouds to provide horizontal and
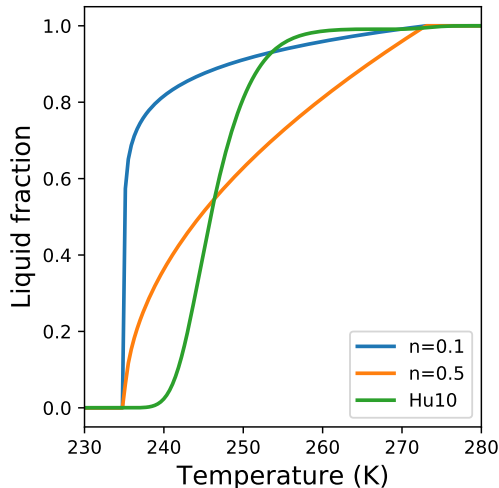
Figure 1. Liquid fraction $\lambda(T)$ as a function of temperature T used in one-moment bulk microphysics scheme, where n is the exponent in the liquid fraction equation (1). Blue curve shows liquid fraction with default value of $n = 0.1$ in Kaul et al. (2015). Orange curve shows liquid fraction with $n = 0.5$, which is used in this study. The green curve shows the empirical liquid fraction from Hu et al. (2010).

vertical advection of heat and moisture as forcing terms in the LES. Therefore, we can treat each LES as an idealized single GCM column, with turbulent fluxes resolved rather than being parameterized. The simplification in radiation allows the two models to achieve closed energy budgets easily so that they have energetically consistent, though not necessarily realistic, mean state climates.

We address the following questions: Can we reproduce and explain the observed seasonal cycle of Arctic clouds with our approach? How is the seasonal cycle influenced by large-scale advection and surface fluxes? Using our framework, we found a robust connection between the seasonal cycle of large-scale advection and polar liquid-containing clouds. In what follows, we describe the modeling setup (section 2), followed by results (section 3), discussion (section 4), and conclusions (section 5).

2 Model Setup

2.1 GCM

We use an idealized moist GCM to simulate large-scale dynamics of an Earth-like atmosphere (Frierson et al., 2006, 2007; O'Gorman & Schneider, 2008). The GCM solves the hydrostatic primitive equation with T42 spectral resolution in the horizontal and 32 unevenly spaced vertical sigma levels. The lower boundary of the GCM is a 5-m thick mixed-layer ocean, and the surface energy budget is closed so that evaporation changes are constrained energetically by changes in other surface energy fluxes. Clouds are not represented in the GCM. Any grid-scale supersaturation is removed immediately to precipitation, and there is no reevaporation of condensate. The GCM uses a two-stream semigray radiation scheme with prescribed longwave and shortwave absorber profiles, as described in O'Gorman and Schneider (2008). We set the longwave optical thicknesses at the equator to $\tau_e = 7.2$ and at the pole to $\tau_p = 1.8$. The optical thickness varies with latitude but does not interact with the water vapor nor cloud condensates of the atmo-

sphere. Therefore, the GCM does not capture the interaction of water vapor and clouds with radiative transfer. The default surface albedo in the aquaplanet configuration is 0.38, but in our case, we set the surface albedo to 0.3 for open water, and to 0.5 for sea ice. The surface roughness length is set to 5×10^{-3} m for momentum, and to 1×10^{-3} m for scalars.

One modification of the GCM specific to the current study is the saturation vapor pressure calculation. In order to obtain consistent thermodynamics, especially at low temperatures, we implemented a look-up table in the GCM to get saturation vapor pressure and its temperature derivatives, instead of using the default formulation in O'Gorman and Schneider (2008). The look-up table is obtained by integrating the Clausius-Clapeyron equation with specific latent heats that depend on temperature (see Equation (1) below). At GCM runtime, the values are determined by linearly interpolating the closest look-up table values. This treatment of saturation vapor pressure is consistent with the LES used in this study (Pressel et al., 2015).

We run the GCM with an obliquity of 23.5°, zero orbital eccentricity, and a seasonal cycle that has a period of 200 days per year. The seasonal cycle is shortened in order to reduce the computational cost of the LES simulations. We refer to the four seasons as the corresponding 50-day averages (e.g., spring is the first 50 days, summer is day 51–100, etc.). We run the GCM for 11 years into an approximate statistical equilibrium and use the last year to provide forcing for the LES.

2.2 LES

We work with the Python Cloud Large Eddy Simulation code (PyCLES) (Pressel et al., 2015). The model uses an anelastic framework, which ensures closed total water specific humidity q_t and specific entropy s budgets. PyCLES has been used successfully to simulate subtropical marine BL clouds (Tan et al., 2016, 2017; Pressel et al., 2017; Schneider et al., 2019), deep convective clouds (Shen et al., 2020), and Arctic mixed-phase stratocumulus (Zhang et al., 2020).

We use a one-moment mixed-phase microphysics scheme that follows Kaul et al. (2015) and solves prognostic equations for snow and rain water specific humidity (q_{snow} and q_{rain}) separately. Cloud condensates are diagnosed through a saturation adjustment procedure from q_t. To partition the total condensate (saturation excess) between liquid and ice, we use a phase partition function that depends on temperature T alone

$$\lambda(T) = \begin{cases} 0 & \text{for } T < T_{\mathrm{cold}}, \\ \left(\dfrac{T - T_{\mathrm{cold}}}{T_{\mathrm{warm}} - T_{\mathrm{cold}}} \right)^n & \text{for } T_{\mathrm{cold}} \leq T \leq T_{\mathrm{warm}}, \\ 1 & \text{for } T_{\mathrm{warm}} < T, \end{cases} \tag{1}$$

where $T_{\mathrm{warm}} = 273$ K and $T_{\mathrm{cold}} = 235$ K are the threshold temperatures for homogeneous melting and freezing (Kaul et al., 2015). The exponent n in the liquid fraction λ is taken to be 0.5 (instead of 0.1, a typically used value for Arctic stratocumulus, see Kaul et al. (2015) and Zhang et al. (2020)). The corresponding liquid fraction is shown in Figure 1. Also plotted for comparison is the observationally-derived curve from Hu et al. (2010). Using the latter does not change the simulated seasonal cycle of clouds qualitatively (Figure S1–S3), as will be discussed in section 4.3.

The cloud liquid droplet number is determined by a prescribed cloud condensation nuclei concentration of 10^8 m^{-3}. Cloud ice, snow, and rain droplet numbers are determined by their particle size distribution function (PSDF) in exponential forms. In order to reduce the number of free parameters, we use diagnostic relationships for rain and snow PSDF intercept parameters. Because it is difficult to measure small ice particles (e.g., McFarquhar et al., 2007), we use 1×10^7 m^{-4} (a default value for Arctic stratocumulus) for the cloud ice PSDF intercept parameter. Because the simulations are not lim-

ited to Arctic BL clouds, we modified the PSDF formulations in the microphysics scheme to be applicable to tropospheric clouds. The intercept parameter of the PSDF for snow uses the default formulation in Grabowski (1998) instead of the empirical expression in H. Morrison et al. (2011) (see also Appendix A in Kaul et al. (2015)). The intercept parameter of the snow PSDF follows the expression in Sekhon and Srivastava (1970).

The LES uses the same radiation scheme as the GCM. Because the LES reference pressure can differ substantially from the GCM pressure at the same altitude, we use the GCM pressure and air density to calculate the radiative tendency in the LES. All LES simulations were conducted with a horizontal resolution of 400 m and a vertical resolution that varies from 74 m near the surface to 420 m at the domain top. Doubling the vertical and horizontal resolutions separately has minimal impact on simulated liquid and ice water paths (Figure S4 and S5). The LES domain is 25.6 km × 25.6 km in the horizontal dimension and 18 km in the vertical dimension. A sponge layer of 6 km at the top of the domain is implemented to damp the velocity and scalar fluctuations toward the domain-mean values. Simulated clouds below 10 km are insensitive to the sponge layer depth. Therefore, we focus on the representation of the bottom 10 km of the model domain. Like the idealized GCM, the lower boundary of LES is a 5-m thick mixed-layer ocean with closed surface energy budget. Surface albedo in the LES is the same as in the GCM: 0.3 for open water, and 0.5 for sea ice.

2.3 Sea Ice Model

We implemented a thermodynamic sea ice model similar to the Semtner (1976) "zero layer" model. This model was initially developed for a GCM, but we now have implemented it in the LES too; however, we prescribe ice thickness in the LES using the GCM output (see Section 2.5). This treatment approximates the specific heat of the ice to be negligible, which implies that the temperature profile within the sea ice remains linear. The present model differs from Semtner (1976) in that for simplicity the freshwater value for the freezing point, $T_{\mathrm{m}} = 273.16$ K, is used at the surface and base of the ice, and a constant latent heat of fusion of ice of $L_{\mathrm{i}} = 3.0 \times 10^8$ J m^{-3} is adopted. Sea ice grows at the base in winter, and ablation occurs at both the surface and the base in summer. There is no surface snow layer and no horizontal sea ice motion.

Where the surface is ice covered ($h_{\mathrm{i}} > 0$), the sea ice thickness evolves according to

$$L_{\mathrm{i}}\frac{dh_{\mathrm{i}}}{dt} = F_{\mathrm{atm}} - F_{\mathrm{base}}. \tag{2}$$

Here the flux exchange between surface and atmosphere F_{atm} includes radiation and turbulent sensible and latent heat fluxes (F_{rad}, F_{SH}, and F_{LH}, respectively), defined to be positive upward,

$$F_{\mathrm{atm}} = F_{\mathrm{rad}} + F_{\mathrm{SH}} + F_{\mathrm{LH}}. \tag{3}$$

The basal heat flux F_{base} from the ocean mixed layer into the ice is taken to depend linearly on the temperature gradient between the mixed layer (at T_{ml}) and the ice base (at the melting temperature T_{m}),

$$F_{\mathrm{base}} = F_0(T_{\mathrm{ml}} - T_{\mathrm{m}}),$$

using the coefficient $F_0 = 120$ W m^{-2} K^{-1} as in Eisenman (2007). The surface temperature of the ice T_{s} is determined implicitly by a balance between the surface flux F_{atm} (which is a function of T_{s}) and the conductive heat flux through ice F_{i},

$$F_{\mathrm{atm}} = F_{\mathrm{i}} = k_{\mathrm{i}}\frac{T_{\mathrm{m}} - T_{\mathrm{s}}}{h_{\mathrm{i}}},$$

where $k_{\mathrm{i}} = 2$ Wm^{-1}K^{-1} is the thermal conductivity of sea ice, except where this gives $T_{\mathrm{s}} > T_{\mathrm{m}}$, in which case instead we set
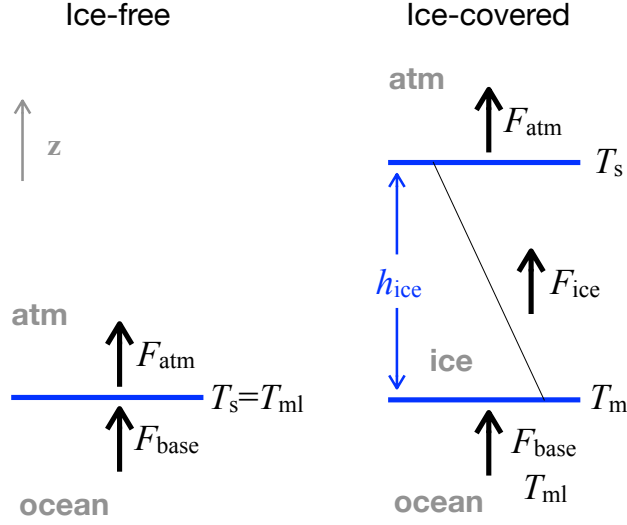
$$T_{\mathrm{s}} = T_{\mathrm{m}},$$

Figure 2. Schematic of the surface boundary conditions. In the GCM, the sea ice specific heat is taken to be zero, so that the temperature profile within the ice is linear. See section 2.3 for details.

representing surface melt (Eisenman & Wettlaufer, 2009).

The ocean mixed-layer temperature T_{ml} is determined by

$$\rho_{\mathrm{w}} c_{\mathrm{w}} h_{\mathrm{ml}} \frac{dT_{\mathrm{ml}}}{dt} = -F_{\mathrm{atm}} \tag{4}$$

under ice-free conditions and

$$\rho_{\mathrm{w}} c_{\mathrm{w}} h_{\mathrm{ml}} \frac{dT_{\mathrm{ml}}}{dt} = -F_{\mathrm{base}} \tag{5}$$

where ice is present. Here ρ_{w} is the density of water, c_{w} is the specific heat of water, and h_{ml} is the constant ocean mixed-layer thickness. The representations of the surface fluxes (F_{rad}, F_{SH}, and F_{LH}) do not explicitly depend on whether the surface is ice-covered or ice-free, although they do depend on the surface temperature.

The transition from ice-free to ice-covered conditions happens when T_{ml} cools below T_{m} during a GCM time step, in which case frazil ice growth is represented by setting $T_{\mathrm{ml}} = T_{\mathrm{m}}$ and assigning a positive tendency to h_{i} equal to this change in T_{ml} scaled by $L_{\mathrm{i}}/(\rho_{\mathrm{w}} c_{\mathrm{w}} h_{\mathrm{ml}})$. Similarly, a transition from ice-covered to ice-free conditions occurs when h_{i} reaches zero, at which point any additional net energy flux warms T_{ml}.

Note that because there is no lateral ocean energy flux ("Q flux") in the present setup, T_{ml} remains at T_{m} where ice is present, causing $F_{\mathrm{base}} = 0$.

2.4 Large-Scale Forcing in LES

In order to include large-scale dynamics in the limited-domain of LES, we use time-varying large-scale fluxes simulated by the GCM to drive the LES for one year (200 simulation days). The details of the forcing framework are described in Shen et al. (2020). In summary, we use LES to simulate a single grid column of a GCM, but with processes that are parameterized in the GCM (e.g., convection, condensation, and BL turbulence)

resolved in the LES. The forcing terms include horizontal and vertical advection of temperature and specific humidity, as well as temperature tendencies due to numerical damping and spectral filtering in the GCM. By doing so, we can avoid nudging of thermodynamic variables in the atmosphere, which is often used to prevent LES from diverging from GCMs but constrains the turbulence development in the LES.

A major distinction between our forcing framework and that of Shen et al. (2020) is the time-varying forcing. Instead of using the long-term mean tendencies, we use the instantaneous tendencies from the GCM, updated every 6 hours. Therefore, the horizontal advective q_t source term S_{hadv} becomes

$$S_{\mathrm{hadv}} = -\tilde{u}\partial_x \tilde{q}_t - \tilde{v}\partial_y \tilde{q}_t, \tag{6}$$

and the vertical advective q_t source term S_{vadv} becomes

$$S_{\mathrm{vadv}} = -\tilde{w}\partial_z q_t. \tag{7}$$

Tildes $\tilde{(\cdot)}$ denote variables resolved on the GCM grid.

Like for the specific humidity, the horizontal advective temperature tendency J_{hadv} is taken directly from the GCM,

$$J_{\mathrm{hadv}} = -\tilde{u}\partial_x \tilde{T} - \tilde{v}\partial_y \tilde{T}, \tag{8}$$

and the vertical advective temperature tendency J_{vadv} becomes

$$J_{\mathrm{vadv}} = -\tilde{w}\partial_z T - \tilde{w}\frac{g}{c_p}, \tag{9}$$

where g is the gravitational acceleration, and c_p is the specific heat of dry air. The source terms (6) and (7) are included in the prognostic equation for total water specific humidity q_t, and the source terms (6)–(9) are included in the prognostic equation for specific entropy s (Shen et al., 2020).

For horizontal momentum forcing (u and v), we impose the GCM-resolved horizontal momentum tendencies on the LES momentum equations. This also differs from Shen et al. (2020), where the GCM large-scale pressure gradient is imposed.

The forcing fields are taken from GCM grid boxes closest to 70°N. This has more relevance for the Arctic Ocean, given the aquaplanet nature of the idealized GCM. To include synoptic-scale variability, we choose four grid points (0°, 90°, 180°, and 270° longitude) instead of using zonal-mean fields from the GCM. The results we present are averages of the 4 simulated locations, which are statistically identical. We call this average the ensemble mean.

2.5 Surface Forcing in LES

To have consistent surface states, we prescribe sea ice thickness in PyCLES from GCM output, updated every 6 hours. This ensures consistent bottom boundary conditions in the GCM and LES, and it indirectly constrains the turbulent heat fluxes. Surface heat fluxes and temperatures are calculated interactively in the LES, thus slight differences are present between the LES and GCM. We have tested directly prescribing surface turbulent heat fluxes instead of sea ice thickness, which led to unreasonable air temperatures in the LES near the surface. We find that prescribing sea ice thickness is a good compromise to obtain comparable surface conditions in the GCM and LES.

3 Results

3.1 Seasonal Cycle

The high-frequency forcing introduces a large amount of variability in the LES simulations. Since we are interested in the seasonal evolution and for better visualization,
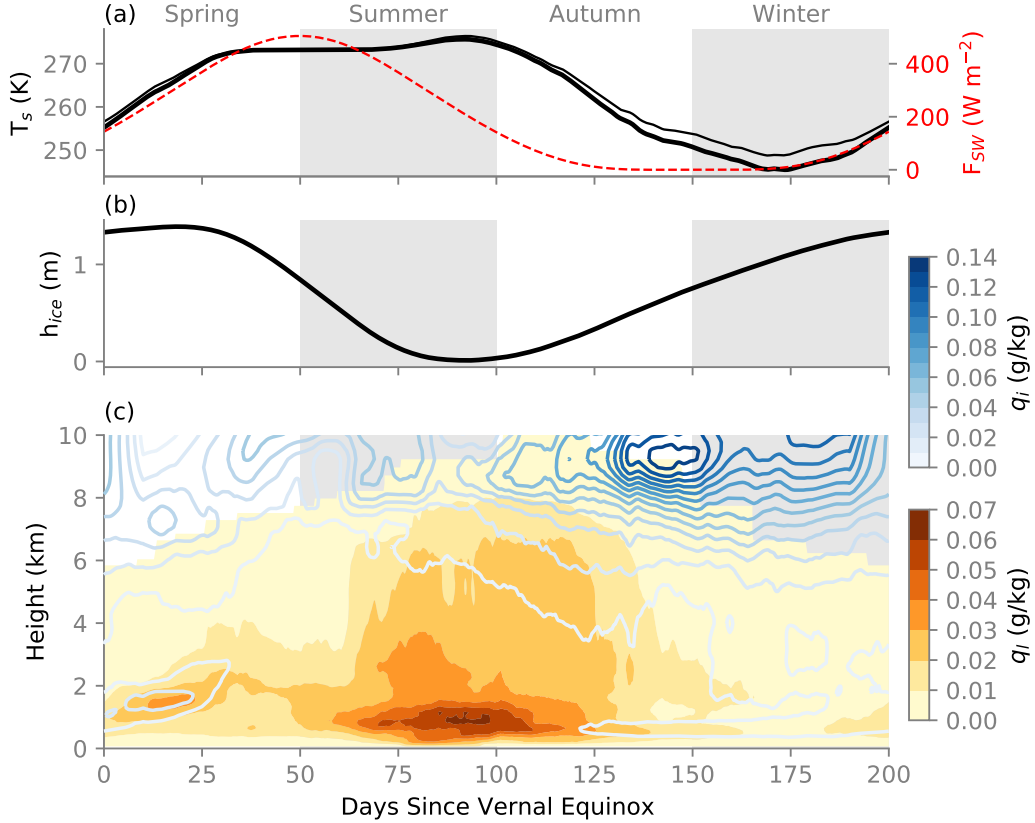
Figure 3. LES ensemble-mean seasonal cycle of domain-mean (a) surface temperature (black thick line) and top-of-atmosphere (TOA) downward shortwave radiative flux (red dashed line), (b) sea ice thickness, and (c) cloud condensate profiles (filled colors for liquid, contours for ice). GCM surface temperature is shown as the black thin line. Data are smoothed by a 20-day running mean.

we apply a 20-day running mean to smooth the high-frequency 6-hourly LES output. Figure 3 shows the seasonal cycle of the surface state and cloud water specific humidities from the GCM-forced LES. Also shown is the insolation forcing at top-of-atmosphere (TOA), which corresponds well with the increase of surface temperature T_s from mid winter to mid spring when ice thickness h_i reaches its maximum of 1.4 m (Figure 3a and 3b), qualitatively consistent with observations over an ice-covered Arctic (Persson, 2002). As T_s reaches the melting temperature, all shortwave forcing is used to melt the sea ice, and h_i declines into summer. Then T_s increases again above the melting temperature, but quickly decreases as insolation declines and sea ice thickens into winter. Overall, there is a good agreement between LES and GCM T_s, with the largest difference of 5 K in winter. The annual variation of T_s is about 30 K, well within the observed range (26–36 K) of the annual variation of monthly-mean near-surface temperatures in the Arctic (Persson, 2002).

The maximum cloud liquid specific humidity q_l is found within the BL during summer and autumn, when T_s is high and h_i is low (Figure 3c). This is also when liquid-containing cloud top reaches the highest vertical extent at about 8 km. The liquid specific humidity q_l is consistently above 0.01 g/kg in spring and drops below 0.01 g/kg during winter. Cloud ice specific humidity q_i, on the other hand, reaches its maximum in late au-
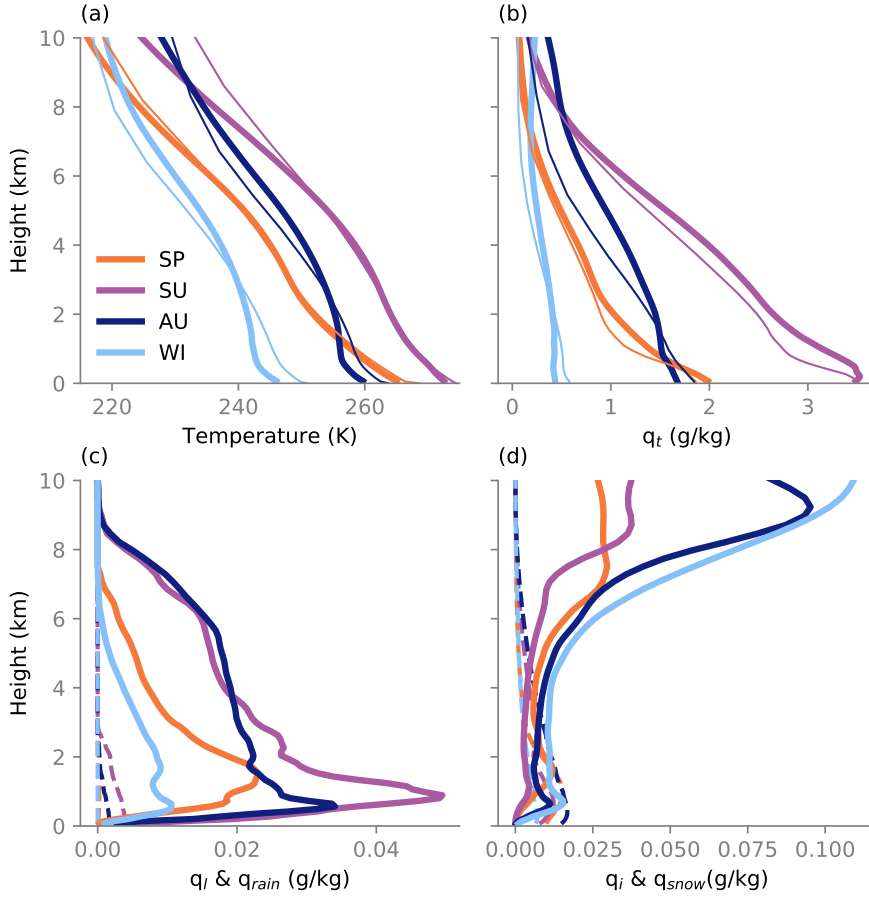
Figure 4. Spring (SP), summer (SU), autumn (AU), and winter (WI) domain-mean profiles averaged over 50 simulation days. (a) Temperature in LES in thick lines and GCM in thin lines. (b) Total water specific humidity in LES in thick lines and GCM in thin lines. (c) LES liquid specific humidity in solid lines and rain specific humidity in dashed lines. (d) LES ice specific humidity in solid lines and snow specific humidity in dashed lines.

tumn in the upper troposphere, and it is present throughout the year. In winter, liquid-containing cloud is still present in the BL, though cloud water specific humidity is dominated by q_i (Figure 4 and S6). The general pattern of the simulated seasonal cycle resembles that of the observed liquid-containing Arctic clouds (Cesana et al., 2012), which is further discussed in section 4.1.

In order to understand the seasonal variability of cloud water profiles, we examine the thermodynamic profiles simulated by both the idealized GCM and the LES (Figure 4). In addition to the large differences in the temperature across the seasons, also the static stability experiences large seasonal variability (Figure 4a). Although there is no temperature inversion in the BL due to the lack of cloud-top radiative cooling, the lower troposphere is more stable in autumn and winter when insolation is weaker, and is more convective in spring and summer when insolation is stronger. The highest specific humidity is found in the summer BL, while the BL is significantly moister in spring and autumn than in winter (Figure 4b).
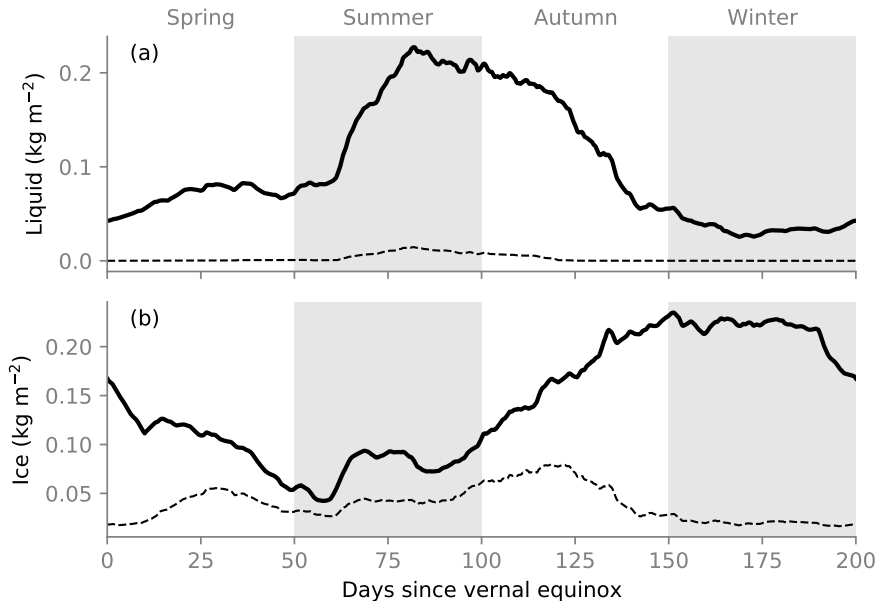
Figure 5. Seasonal cycle of ensemble-mean (a) liquid water path (solid) and rain water path (dashed), and (b) ice water path (solid) and snow water path (dashed). Data are smoothed by a 20-day running mean.

The corresponding seasonally-averaged cloud water profiles also display large variability. The liquid specific humidity q_l peaks in the lower troposphere below 2 km throughout the year: the summer peak value is five times the winter peak value (Figure 4c). The q_l peaks at 1 km in summer and autumn further indicate the presence of the stratiform layers (also apparent in Figure 3c). In contrast, ice specific humidity q_i peaks in the upper troposphere, and maximizes in winter (Figure 4d). Rain is negligible, but there is a significant amount of snow in the lower troposphere, with a magnitude that is comparable to q_i.

Radiatively, the seasonal cycle of condensed water path (the vertical integral of cloud water specific humidity) is a major factor in determining the CRE. Figure 5 shows the cloud liquid water path (LWP), ice water path (IWP), rain water path, and snow water path integrated over the lower 10 km of the LES domain. LWP exhibits a seasonal cycle with a maximum of 0.25 kg m^{-2} in summer and a minimum of 0.03 kg m^{-2} in winter (Figure 5a). IWP shows a shifted seasonal cycle that maximizes at 0.25 kg m^{-2} in winter (Figure 5b). Intuitively, we expect higher LWP in the summer and higher IWP in the winter, due to the temperature dependency of the liquid fraction shown by equation (1). The snow water path maximizes in autumn and always exceeds the rain water path.

3.2 Estimating Cloud Radiative Effects

Although the gray radiation scheme does not allow cloud-radiation interactions in either the GCM or the LES, we use an offline radiative transfer model to estimate the radiative effects of the clouds in the LES. To do so, we use the Rapid Radiative Transform Model for GCMs (RRTMG) (Iacono et al., 2008). Domain-mean profiles of 6-hourly temperature, specific humidity, pressure, density, and cloud water specific humidity from LES are used as input fields for RRTMG. Above the LES domain, we patch temperature, specific humidity, and pressure profiles from the "Arctic profile" given for the Mixed-

346 Phase Arctic Cloud Experiment intercomparison (Klein et al., 2009; Kaul et al., 2015).
347 We define the longwave (LW) and shortwave (SW) CREs as the difference between net
348 all-sky fluxes and clear-sky fluxes, either at TOA or at the surface (SFC):

$$\mathrm{LWCRE} = (\mathrm{LW}_{\mathrm{all-sky}}^{\downarrow} - \mathrm{LW}_{\mathrm{all-sky}}^{\uparrow}) - (\mathrm{LW}_{\mathrm{clear}}^{\downarrow} - \mathrm{LW}_{\mathrm{clear}}^{\uparrow}), \tag{10}$$

$$\mathrm{SWCRE} = (\mathrm{SW}_{\mathrm{all-sky}}^{\downarrow} - \mathrm{SW}_{\mathrm{all-sky}}^{\uparrow}) - (\mathrm{SW}_{\mathrm{clear}}^{\downarrow} - \mathrm{SW}_{\mathrm{clear}}^{\uparrow}), \tag{11}$$

$$\mathrm{CRE} = \mathrm{LWCRE} + \mathrm{SWCRE}. \tag{12}$$

353 The annual-mean CRE at TOA and at SFC are summarized in Figure 6, along with the
354 observed climatological values from CERES-EBAF averaged over 70–75°N. The observed
355 net effect of clouds at TOA is -10 W m^{-2} (i.e., cooling), which is dominated by SWCRE.
356 For the LES, when both cloud liquid and ice are included in the radiative transfer cal-
357 culation, the LWCRE term dominates because there is excessive cloud ice in the upper
358 troposphere in our simulations (Figure 6a). If we only include cloud liquid in the cal-
359 culation, TOA LWCRE decreases from 33 to 16 W m^{-2}, and the annual-mean net CRE
360 is much closer to observations (Figure 6b). Surface CRE is not as sensitive to upper-tropospheric
361 cloud ice, since cloud liquid in the lower troposphere is already optically thick. The annual-
362 mean SFC CREs match the observed values well, with or without cloud ice (Figure 6c
363 and 6d). Although the agreement between observations and liquid-only CRE is coinci-
364 dental, the observed annual-mean CRE of ice clouds is small at high latitudes (Hong et
365 al., 2016). We focus here on the seasonal cycle of liquid-only CREs and defer the dis-
366 cussion on cloud ice bias to Section 4.

367 Figure 6b and 6d shows the seasonal cycle of CRE at TOA and SFC using cloud
368 liquid only in the RRTMG calculations. The ensemble mean CRE is the average of 4 of-
369 fline radiative transfer calculations from each LES simulation (as opposed to the offline
370 calculation of the ensemble mean clouds). The seasonal cycle of TOA CRE is dominated
371 by the seasonality in SWCRE: Clouds have a strong cooling effect during the sun-lit part
372 of the year; during polar night, their longwave warming effect dominates, as expected
373 (Figure 6a). The TOA LWCRE has a muted seasonal cycle and peaks in late summer/early
374 autumn. It depends on the difference between $\mathrm{LW}_{\mathrm{all-sky}}^{\uparrow}$ and $\mathrm{LW}_{\mathrm{clear}}^{\uparrow}$. While $\mathrm{LW}_{\mathrm{clear}}^{\uparrow}$ varies
375 little from mid-summer to early autumn, $\mathrm{LW}_{\mathrm{all-sky}}^{\uparrow}$ decreases as cloud top temperature
376 drops (not shown), maximizing LWCRE during this time. At SFC, the LWCRE seasonal
377 cycle is damped compared to TOA; SWCRE variability is weaker at the surface than at
378 TOA, but still peaks in late spring (Figure 6b). The net CRE at the surface is much higher
379 than at TOA (15 versus -13 W m^{-2}), suggesting that polar clouds warm the surface
380 in our LES.

4 Discussion

4.1 Comparison to Observations

383 An encouraging result of our experiment is the resemblance of the simulated liquid-
384 containing clouds to observations. Although the model setup here is highly idealized, many
385 processes are absent, and detailed reproduction of the seasonal cycle is not a goal, the
386 simulated seasonal cycle of clouds and CRE still resembles that observed. This suggests
387 that elements that are essential for producing the observed seasonal cycle of Arctic clouds
388 are present in our idealized setup. For example, Cesana et al. (2012) produced the sea-
389 sonal cycle of cloud fraction averaged over the Arctic Ocean (70–82°N) based on a space-
390 borne lidar (CALIPSO-GOCCP). They found the maximum frequency of occurrence of
391 liquid-containing clouds near the surface from May to September, and the liquid-containing
392 cloud reaches is maximum vertical extent at 7.5 km altitude in July. During winter, the
393 liquid-containing cloud fraction is lower, but still persistent below 2 km. Ice-dominated
394 cloud fraction is lower than liquid overall, and is zero below 4 km during June to Au-
395 gust. The ice-dominated cloud fraction maximum occurs at 7 km in winter, while it reaches
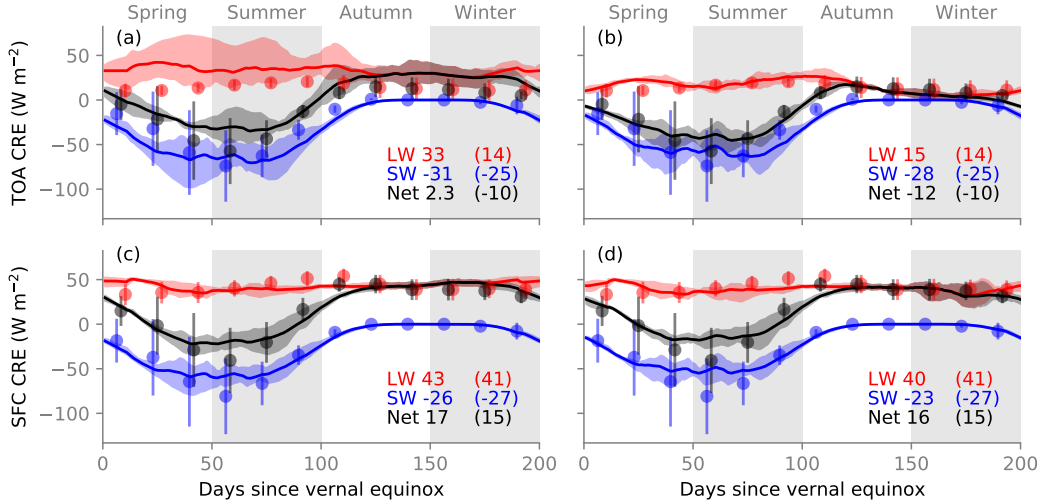396 as high as 11 km. These observations match well with the simulated seasonal cycle of

Figure 6. Offline RRTMG calculation of CRE at (a)-(b) TOA and (c)-(d) SFC using domain-mean profiles from LES. Left column shows calculation with cloud liquid and ice, right column shows calculation with cloud liquid only. Ensemble mean CREs are in solid lines. Shading shows the minimum and maximum range within the ensemble. Data are smoothed by a 20-day running mean. Annual mean CRE values are shown in the lower right. Dots show the observed CERES-EBAF CRE monthly climatology averaged over 70–75°N, and error bars show the spatial standard deviation for each month. Annual mean CRE values from observations are shown in parentheses.

clouds in our LES (Figure 3c). However, it should be borne in mind that direct comparisons between LES and observations are difficult because the spatial scales and definitions of cloud fractions are different in LES and in satellite-derived observations in Cesana et al. (2012). A more sophisticated comparison should involve satellite simulators that convert simulated thermodynamic fields to variables that are directly measured by satellites (Chepfer et al., 2008; Kay et al., 2016). Nonetheless, the similarity of the LES to observations provides evidence for the physical relevance of our experiments.

Next, we compare the condensed water paths with satellite observations over the Arctic Ocean north of 60°N (Figure 2 in Lenaerts et al. (2017)). The observed LWP ranges from 0.015 to 0.125 kg m^{-2}, with the maximum occurring during late summer and the minimum during winter. Although the maximum ensemble-mean LWP during summer in our LES is over-estimated (0.22 kg m^{-2}), the timing of the maximum and minimum is consistent with the observed LWP in polar oceans (Figure 5a). Larger discrepancies are found in IWP. The observed IWP over the Arctic Ocean ranges from 0.01 to 0.11 kg m^{-2}. In the LES, the ensemble-mean IWP ranges from 0.07 to 0.4 kg m^{-2} (Figure 5b), much higher than observed. The seasonal cycle of IWP is weak in observations, and our results show a peak in IWP during winter. The cloud ice excess in the LES may be related to our simple treatment of ice microphysics and an inefficient removal of ice particles at high altitudes. Interestingly, comprehensive climate models tend to overestimate LWP and underestimate IWP (Zuidema & Joyce, 2008; Lenaerts et al., 2017).

Being aware of the biases in our simulated cloud water fields, we compare our estimated liquid-only CRE to observations from Clouds and the Earth's Radiant Energy System Energy Balanced and Filled (CERES-EBAF, Loeb et al., 2017; Kato et al., 2018). We choose the latitude band 70–75°N to get average observed radiative fluxes. The se-
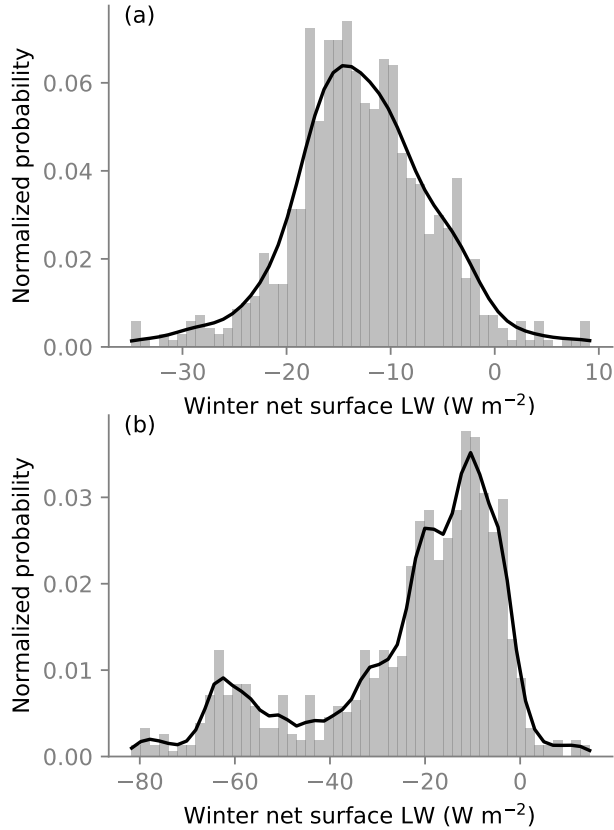
Figure 7. Normalized histogram (gray) and probability distribution (black line) of winter net surface longwave fluxes from offline RRTMG calculations using LES simulations. (a) Cloud liquid and ice are included. (b) Only cloud liquid is included.

421 lected domain covers the seasonal sea ice edge, providing the relevant comparison to our
422 idealized experiment. Monthly data from CERES-EBAF are scaled in time to match the
423 accelerated seasonal cycle of our LES (Figure 6). The observed SWCRE shows high spa-
424 tial standard deviations during sunlit months, but the observed LWCRE shows low spa-
425 tial standard deviations in warmer months. As a result, our simulated SWCRE is gen-
426 erally within the observed range during the highly variable spring and early summer months
427 (Figure 6b). Our simulated TOA LWCRE is too strong in spring, and TOA SWCRE is
428 stronger in late summer/early autumn compared to CERES-EBAF. Nonetheless, our sim-
429 ulated annual-mean TOA LWCRE and SWCRE based on cloud liquid alone agree well
430 with observations. Note that when cloud ice is included, TOA LWCRE shows larger vari-
431 ability across ensemble members throughout the year. Although the minimum LWCRE
432 agrees with CERES in summer and autumn, the annual mean LWCRE and net CRE are
433 much higher than observed.

434   A unique feature of the Arctic is the presence of two preferred states in the win-
435 ter BL: a cloudy and a clear state. This is a robust feature in field observations and re-
436 analysis, but often misrepresented in comprehensive climate models (Pithan et al., 2014,
437 2016). Therefore, it is encouraging that our idealized LES can produce a bi-modal dis-
438 tribution of the winter liquid-only net SFC LW fluxes (Figure 7b). The main peak is found
439 around -20 to 0 W m^{-2}, corresponding to the cloudy state that GCMs often miss. The
440 secondary peak is found around -60 W m^{-2}, corresponding to the clear state. When both
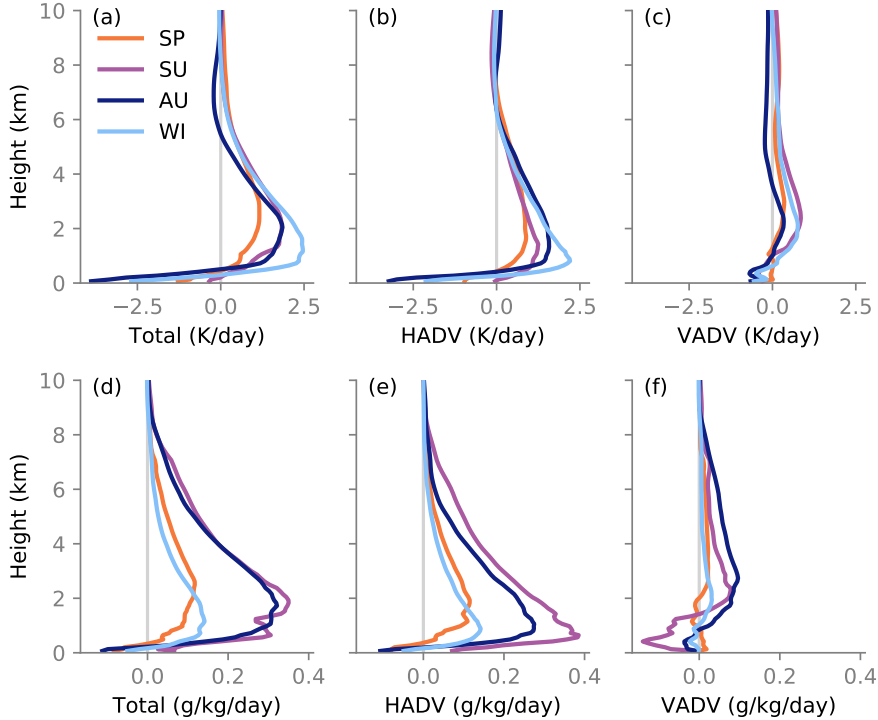
Figure 8. LES spring (SP), summer (SU), autumn (AU), and winter (WI) domain-mean profiles averaged over 50 simulation days. (a) Total temperature advection. (b) Horizontal temperature advection. (c) Vertical temperature advection. (d) Total specific humidity advection. (e) Horizontal specific humidity advection. (f) Vertical specific humidity advection. Horizontal advection (HADV) is taken directly from the GCM, while vertical advection (VADV) is a hybrid of GCM and LES fields.

cloud liquid and ice are included in radiative transfer calculations, we see only one peak around -14 W m^{-2} (Figure 7a), highlighting the positive cloud ice bias. Our modeling framework can serve as a tool to study such air mass transformation in the Arctic (Pithan et al., 2016).

4.2 Forcing and Clouds

What determines the seasonal cycle of Arctic liquid-containing clouds? We compare the two external non-radiative forcings in our LES: large-scale advection and surface heat fluxes. Because large-scale advection is prescribed in the LES, it does not interact with the thermodynamic and cloud fields, therefore directly influencing cloud water amount. Although surface turbulent heat fluxes are not prescribed in the LES, they are indirectly controlled by the prescribed sea ice thickness. Therefore, we consider them as a part of the forcing that affects the simulated clouds.

Large-scale advection is more important at high latitudes than at lower latitudes because atmospheric heat transport balances the net negative radiative forcing at TOA (Serreze et al., 2007). Large-scale advection brings heat and moisture into the high latitudes year-round (Figure 8a and 8d). For both temperature and specific humidity advection, the horizontal advection terms dominate (Figure 8b and 8e). Temperature advection is the strongest in winter, when the pole-to-equator temperature gradient is the strongest. Summer temperature advection is weak, but it is associated with the largest
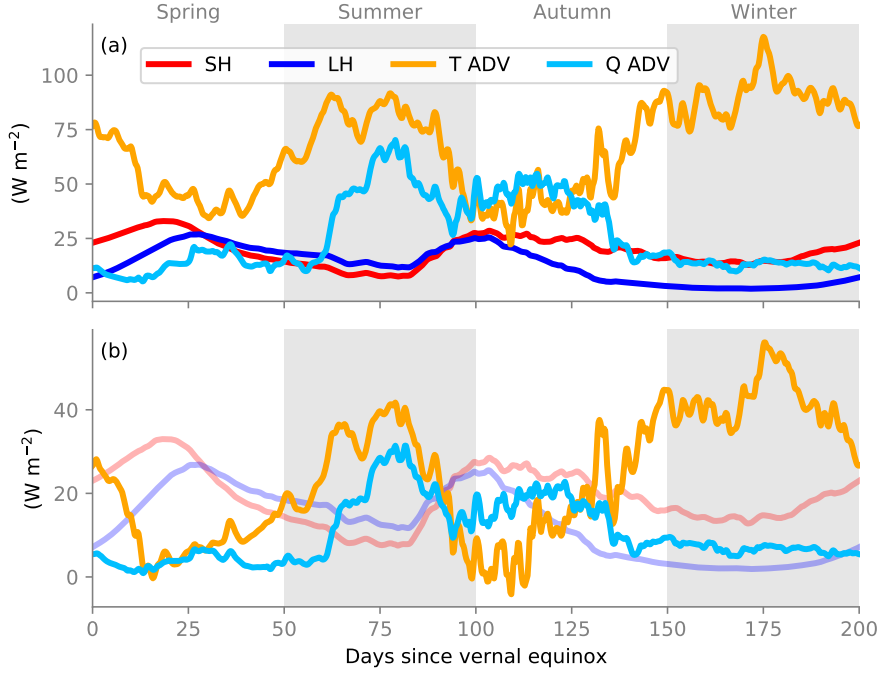
Figure 9. (a) Seasonal cycle of total temperature and specific humidity advection (T ADV and Q ADV, vertically integrated over the entire domain, converted to dry and latent energy fluxes), as well as sensible heat (SH) and latent heat (LH) fluxes at the surface. (b) Seasonal cycle of total temperature and specific humidity advection integrated over the bottom 2 km. Data are smoothed by a 20-day running mean.

specific humidity advection. On the other hand, specific humidity advection is weak in winter and spring, contributing to a polar troposphere that is cold and dry. The specific humidity advection seasonal cycle is consistent with the observed horizontal specific humidity advection north of $70°$N, but our simulations have peak values in summer that are twice the reanalysis values (Serreze et al., 2007; Newman et al., 2012).

In order to compare the magnitudes of large-scale advection and surface heat fluxes, we integrate the large-scale advection vertically for the entire LES domain and for the BL (Figure 9). Throughout the year, large-scale advection dominates the forcing budget for both temperature and moisture, especially in the summer (Figure 9a). The only exception is in spring, where surface latent heat flux is larger than specific humidity advection. However, if we focus on the BL (lowest 2 km, Figure 9b), surface heat fluxes are of comparable magnitudes and exceeds large-scale advection in spring and early autumn.

The concurrence of the specific humidity advection peak and cloud liquid maximum (Figure 9a and 5a) points to the dominant role that large-scale specific humidity advection plays in governing the seasonal cycle of cloud liquid in the polar region. In summer, air temperatures continue to rise and so does the saturation specific humidity. A moisture source is needed for condensation to occur during this warm period, and in our case the source comes from large-scale advection of water vapor (surface latent heat flux reaches a local minimum). Air temperatures begin to decrease at the end of summer, which lowers the saturation specific humidity. Cloud condensates form in autumn due to both cooling and a continuous supply of water vapor from large-scale advection. During this time, increased coupling between the BL and the surface also allows surface evaporation to pro-

vide substantial moisture to form clouds (Kay & Gettelman, 2009; A. L. Morrison et al., 2018). This is evident in Figure 9b: surface latent heat flux exceeds specific humidity advection in the BL in early autumn. In winter, in spite of the cold air temperatures and low saturation specific humidity, large-scale temperature advection maximizes and warms the troposphere, making it harder to form cloud condensates.

Beesley and Moritz (1999) tested the sensitivity to large-scale advection of moisture by swapping summer and winter specific humidity advection in a single-column model. They found little changes in the simulated cloud fraction. However, both liquid and ice water paths were doubled in winter when summer specific humidity advection is applied (roughly doubling the winter specific humidity advection). Their insensitivity of cloud fraction to specific humidity advection may be due to biases in the mean state, such as the lack of high-frequency variability in the forcing.

4.3 Limitations

Although the idealized GCM has been shown to capture many large-scale features of the atmospheric circulation, not all aspects are accurately simulated. Known biases include the jet stream and the storm track's response to warming (e.g., Tan et al., 2019). Furthermore, the GCM used in the study has a positive relative humidity bias in the polar regions. According to reanalysis, the climatological relative humidity in the free troposphere is between 65% and 70% at 70°N. In the idealized GCM, the relative humidity is at least 10% higher. This leads to a moist bias in the LES, manifested in the excessive IWP (Figure 5b) and high ice specific humidity in the upper troposphere (Figure 3c). The lack of continents may partly explain the over-estimated summer specific humidity advection into the polar region, as mentioned in section 4.2. We will address these issues in future updates of the experimental design to improve our understanding of polar cloud dynamics.

Our use of a one-moment bulk microphysics scheme can be limiting in reproducing the observed cloud seasonal cycle, and especially the ice phase. IWP in our LES is about 4 times higher than what is seen in observations over the Arctic Ocean (Lenaerts et al., 2017). While we limited our investigation to the only microphysics scheme that currently contains the ice phase in PyCLES, we tested the sensitivity of our results to the formulation of liquid fraction (Figure 1) by using the observationally derived formula: in Hu et al. (2010), with higher liquid to ice ratio above 246 K, and vice versa below 246 K, the modification in liquid fraction is largest at temperatures around 240 K (Figure S1). With this modification in the LES, we found the largest modification in q_l at temperatures above 240 K because of the exponential nature of the Clausius-Clapeyron relation. As a result, LWP is higher in summer to autumn and lower in winter in the simulation with the Hu et al. (2010) liquid fraction (Figure S2). Its effect on liquid-only CRE is strongest in winter, because there is a cancellation in LW and SW during sunlit seasons. The lowered LWP in winter due to the Hu et al. (2010) liquid fraction leads to a slight reduction of LWCRE, which dominates the net TOA CRE change of -2.4 W m^2 in the annual mean (Figure S3).

The lack of water vapor feedback and cloud radiative effects in our modeling framework becomes a major drawback when it comes to representing details of cloud structures and coupling between radiation and dynamics. For example, cloud-top radiative cooling imposes a dominant forcing to the dynamics of stratocumulus (Bretherton et al., 1999). Without it, the turbulence in the BL is unlikely to be strong enough to produce a well-mixed layer and an inversion above the cloud tops. Cloud-top radiative cooling also provides a mechanism for observed mixed-phase stratocumulus to persist, instead of dissipating through ice precipitation (H. Morrison et al., 2011). Although the turbulent kinetic energy vertical profiles from our simulations are of comparable magnitudes to observations of Arctic BL (Pinto, 1998), the vertical velocity variance tends to be weak.

Lack of this radiation-dynamics coupling explains the structural differences between our simulated clouds and observed Arctic clouds (e.g., the absent of temperature inversions in BL in section 3.1). Furthermore, the absence of an insulating snow layer on sea ice can inhibit the formation of surface-based inversions (Stramler et al., 2011). However, our GCM-forcing framework provides a clean setup to study the role large-scale advection plays in controlling the seasonal cycle of cloud liquid. In a follow-up paper, we will use the same framework to explore the response of polar clouds to climate warming.

5 Conclusions

We adopted an idealized framework in which large eddy simulations are driven by large-scale forcing from a GCM in a high-latitude setting. Our approach encapsulates components of first-order importance in the polar regions, such as large-scale advection of heat and moisture, sea ice, and a simple representation of mixed-phase microphysics. Water vapor feedbacks and cloud radiative effects are not represented in the gray radiative transfer schemes in both the GCM and the LES.

The seasonal cycle of simulated polar clouds resembles observations qualitatively. In particular, maximum cloud liquid specific humidity is found below 2 km in summer and autumn, and minimum is found in winter. Cloud ice specific humidity is the dominant cloud condensate in the upper troposphere. The condensed water path is dominated by IWP, which is overestimated compared to observations. LWP, on the other hand, agrees better with satellite-derived values over the Arctic Ocean. Offline radiative transfer calculations of liquid-only CREs also show encouraging agreement with CERES-EBAF: the net liquid-only CRE is to cool the LES domain, but to warm the surface. Net surface longwave fluxes show a bi-modal distribution of a cloudy and clear state in the winter, providing further agreement with observations qualitatively.

Analysis of the forcing budget points to the dominant role that large-scale advection of moisture plays in controlling the seasonal cycle of cloud liquid. Our study confirms the previous findings by Beesley and Moritz (1999), and further emphasizes that in the BL, surface evaporation is of comparable magnitude to large-scale specific humidity advection. The peak of large-scale temperature advection occurs in winter, when the pole-to-equator temperature gradient is greatest. This warms the polar troposphere and reduces cloud condensates.

Our idealized framework provides an opportunity to study mechanisms of cloud-climate feedbacks that are present in the complex polar climate system. In a follow-on paper, we will look at the polar cloud response to climate warming caused by increased longwave optical thickness of the atmosphere. We will also analyze how changes in large-scale advection with warming affect the simulated cloud amount, to pave the road for future studies with more realistic large-scale forcing from reanalysis and comprehensive GCMs.

tech's High Performing Cluster, which is partially supported by a grant from the Gordon and Betty Moore Foundation.

Data Availability Statement

References

Beesley, J. A., & Moritz, R. E. (1999). Toward an Explanation of the Annual Cycle of Cloudiness over the Arctic Ocean. *Journal of Climate*, *12*, 395–415. doi: 10.1175/1520-0442(1999)012⟨0395:TAEOTA⟩2.0.CO;2

Betts, A. K., & Miller, M. J. (1986). A new convective adjustment scheme. Part II: Single column tests using GATE wave, BOMEX, ATEX and arctic air-mass data sets. *Quarterly Journal of the Royal Meteorological Society*, *112*(473), 693–709. Retrieved 2021-05-11, from `https://rmets.onlinelibrary.wiley.com/doi/abs/10.1002/qj.49711247308` doi: https://doi.org/10.1002/qj.49711247308

Bretherton, C. S., Macvean, M. K., Bechtold, P., Chlond, A., Cotton, W. R., Cuxart, J., ... Wyant, M. C. (1999). An intercomparison of radiatively driven entrainment and turbulence in a smoke cloud, as simulated by different numerical models. *Quarterly Journal of the Royal Meteorological Society*, *125*(554), 391–423. doi: 10.1002/qj.49712555402

Cesana, G., Kay, J. E., Chepfer, H., English, J. M., & de Boer, G. (2012). Ubiquitous low-level liquid-containing Arctic clouds: New observations and climate model constraints from CALIPSO-GOCCP. *Geophysical Research Letters*, *39*. doi: 10.1029/2012GL053385

Chepfer, H., Bony, S., Winker, D., Chiriaco, M., Dufresne, J.-L., & Sze, G. (2008). Use of CALIPSO lidar observations to evaluate the cloudiness simulated by a climate model. *Geophysical Research Letters*, *35*. doi: 10.1029/2008GL034207

Cox, C. J., Uttal, T., Long, C. N., Shupe, M. D., Stone, R. S., & Starkweather, S. (2016). The role of springtime Arctic clouds in determining autumn sea ice extent. *Journal of Climate*, *29*, 6581-6596. doi: 10.1175/JCLI-D-16-0136.1

Curry, J. A., & Herman, G. F. (1985). Relationships between large-scale heat and moisture budgets and the occurrence of Arctic stratus clouds. *Monthly Weather Review*, *113*(9), 1441–1457. doi: 10.1175/1520-0493(1985)113⟨1441:RBLSHA⟩2.0.CO;2

Curry, J. A., Schramm, J. L., Rossow, W. B., & Randall, D. (1996). Overview of Arctic cloud and radiation characteristics. *Journal of Climate*, *9*, 1731-1764. doi: 10.1175/1520-0442(1996)009⟨1731:OOACAR⟩2.0.CO;2

Dal Gesso, S., & Neggers, R. A. J. (2018, February). Can We Use Single-Column Models for Understanding the Boundary Layer Cloud-Climate Feedback? *Journal of Advances in Modeling Earth Systems*, *10*(2), 245–261. doi: 10.1002/2017MS001113

Eisenman, I. (2007). Arctic catastrophes in an idealized sea ice model. In *2006 program of studies: Ice (geophysical fluid dynamics program)* (p. 133-161). Woods Hole Oceanog. Inst. Tech. Rept. 2007-02. (http://www.whoi.edu/page.do?pid=12938)

Eisenman, I., & Wettlaufer, J. S. (2009, January). Nonlinear threshold behavior during the loss of Arctic sea ice. *Proceedings of the National Academy of Sciences*,

106(1), 28–32. doi: 10.1073/pnas.0806887106

Frierson, D. M. W., Held, I. M., & Zurita-Gotor, P. (2006). A gray-radiation aqua-planet moist GCM. Part I: Static stability and eddy scale. *Journal of the Atmospheric Sciences*, *63*, 2548–2566. doi: 10.1175/JAS3753.1

Frierson, D. M. W., Held, I. M., & Zurita-Gotor, P. (2007). A gray-radiation aqua-planet moist GCM. Part II: Energy rransports in altered climates. *Journal of the Atmospheric Sciences*, *64*, 1680–1693. doi: 10.1175/JAS3913.1

Grabowski, W. W. (1998). Toward cloud resolving modeling of large-scale tropical circulations: A simple cloud microphysics parameterization. *Journal of the Atmospheric Sciences*, *55*, 3283-3298.

Hu, Y., Rodier, S., Xu, K.-m., Sun, W., Huang, J., Lin, B., . . . Josset, D. (2010). Occurrence, liquid water content, and fraction of supercooled water clouds from combined CALIOP/IIR/MODIS measurements. *Journal of Geophysical Research*, *115*. (D00H34) doi: 10.1029/2009JD012384

Iacono, M. J., Delamere, J. S., Mlawer, E. J., Shephard, M. W., Clough, S. A., & Collins, W. D. (2008). Radiative forcing by long-lived greenhouse gases: Calculations with the AER radiative transfer models. *Journal of Geophysical Research*, *113*. (D13103) doi: 10.1029/2008JD009944

Karlsson, J., & Svensson, G. (2013). Consequences of poor representation of Arctic sea-ice albedo and cloud-radiation interactions in the CMIP5 model ensemble. *Geophysical Research Letters*, *40*, 4374–4379. doi: 10.1002/grl.50768

Kato, S., Rose, F. G., Rutan, D. A., Thorsen, T. J., Loeb, N. G., Doelling, D. R., . . . Ham, S.-H. (2018, March). Surface Irradiances of Edition 4.0 Clouds and the Earths Radiant Energy System (CERES) Energy Balanced and Filled (EBAF) Data Product. *Journal of Climate*, *31*, 4501–4527. doi: 10.1175/JCLI-D-17-0523.1

Kaul, C. M., Teixeira, J., & Suzuki, K. (2015). Sensitivities in large-eddy simulations of mixed-phase Arctic stratocumulus clouds using a simple microphysics approach. *Monthly Weather Review*, *143*, 4393-4421. doi: 10.1175/MWR-D-14-00319.1

Kay, J. E., & Gettelman, A. (2009). Cloud influence on and response to seasonal Arctic sea ice loss. *Journal of Geophysical Research*, *114*. doi: 10.1029/2009JD011773

Kay, J. E., & L'Ecuyer, T. (2013). Observational constraints on Arctic ocean clouds and radiative fluxes during the early 21st century. *Journal of Geophysical Research*, *118*, 7219–7236. doi: 10.1002/jgrd.50489

Kay, J. E., L'Ecuyer, T., Chepfer, H., Loeb, N., Morrison, A., & Cesana, G. (2016). Recent advances in Arctic cloud and climate research. *Current Climate Change Reports*, *2*(4), 159–169.

Klein, S. A., McCoy, R. B., Morrison, H., Ackerman, A. S., Avramov, A., Boer, G. d., . . . Zhang, G. (2009). Intercomparison of model simulations of mixed-phase clouds observed during the ARM Mixed-Phase Arctic Cloud Experiment. I: single-layer cloud. *Quarterly Journal of the Royal Meteorological Society*, *135*, 979–1002. doi: 10.1002/qj.416

Kretzschmar, J., Salzmann, M., Mlmenstdt, J., & Quaas, J. (2019, August). Arctic clouds in ECHAM6 and their sensitivity to cloud microphysics and surface fluxes. *Atmospheric Chemistry and Physics*, *19*(16), 10571–10589. doi: https://doi.org/10.5194/acp-19-10571-2019

Krueger, S. K. (1988). Numerical simulation of tropical cumulus clouds and their interaction with the subcloud layer. *Journal of the Atmospheric Sciences*, *45*(16), 2221–2250. Retrieved 2021-05-11, from `https://journals.ametsoc.org/view/journals/atsc/45/16/1520-0469_1988_045_2221_nsotcc_2_0_co_2.xml` (Publisher: American Meteorological Society Section: Journal of the Atmospheric Sciences) doi: 10.1175/1520-0469(1988)045⟨2221:NSOTCC⟩2.0.CO;2

Lenaerts, J. T. M., VanTricht, K., Lhermitte, S., & L'Ecuyer, T. S. (2017). Polar clouds and radiation in satellite observations, reanalyses, and climate models. *Geophysical Research Letters*, *44*, 3355–3364. doi: 10.1002/2016GL072242

Liu, Y., Key, J. R., Ackerman, S. A., Mace, G. G., & Zhang, Q. (2012). Arctic cloud macrophysical characteristics from CloudSat and CALIPSO. *Remote Sensing of Environment*, *124*, 159–173. doi: 10.1016/j.rse.2012.05.006

Loeb, N. G., Doelling, D. R., Wang, H., Su, W., Nguyen, C., Corbett, J. G., ... Kato, S. (2017, November). Clouds and the Earths Radiant Energy System (CERES) Energy Balanced and Filled (EBAF) Top-of-Atmosphere (TOA) Edition-4.0 Data Product. *Journal of Climate*, *31*(2), 895–918. doi: 10.1175/JCLI-D-17-0208.1

McFarquhar, G. M., Zhang, G., Poellot, M. R., Kok, G. L., McCoy, R., Tooman, T., ... Heymsfield, A. J. (2007). Ice properties of single-layer stratocumulus during the Mixed-Phase Arctic Cloud Experiment: 1. Observations. *Journal of Geophysical Research*, *112*(D24). Retrieved 2017-12-21, from `http://doi.wiley.com/10.1029/2007JD008633` doi: 10.1029/2007JD008633

Morrison, A. L., Kay, J. E., Chepfer, H., Guzman, R., & Yettella, V. (2018). Isolating the Liquid Cloud Response to Recent Arctic Sea Ice Variability Using Spaceborne Lidar Observations. *Journal of Geophysical Research*, *123*, 473–490. doi: 10.1002/2017JD027248

Morrison, H., Zuidema, P., Ackerman, A. S., Avramov, A., de Boer, G., Fan, J., ... Shipway, B. (2011, February). Intercomparison of cloud model simulations of Arctic mixed-phase boundary layer clouds observed during SHEBA/FIRE-ACE. *Journal of Advances in Modeling Earth Systems*, *3*(2). doi: 10.1029/2011MS000066

Neggers, R. a. J., Siebesma, A. P., & Heus, T. (2012). Continuous single-column model evaluation at a permanent meteorological supersite. *Bulletin of the American Meteorological Society*, *93*(9), 1389–1400. Retrieved 2021-05-11, from `https://journals.ametsoc.org/view/journals/bams/93/9/bams-d-11-00162.1.xml` (Publisher: American Meteorological Society Section: Bulletin of the American Meteorological Society) doi: 10.1175/BAMS-D-11-00162.1

Newman, M., Kiladis, G. N., Weickmann, K. M., Ralph, F. M., & Sardeshmukh, P. D. (2012, May). Relative contributions of synoptic and low-frequency eddies to time-mean atmospheric moisture transport, including the role of atmospheric rivers. *Journal of Climate*, *25*(21), 7341–7361. (Publisher: American Meteorological Society) doi: 10.1175/JCLI-D-11-00665.1

O'Gorman, P. A., & Schneider, T. (2008). The hydrological cycle over a wide range of climates simulated with an idealized GCM. *Journal of Climate*, *21*, 3815–3832. doi: 10.1175/2007JCLI2065.1

Ovchinnikov, M., Ackerman, A. S., Avramov, A., Cheng, A., Fan, J., Fridlind, A. M., ... Sulia, K. (2014). Intercomparison of large-eddy simulations of Arctic mixed-phase clouds: Importance of ice size distribution assumptions. *Journal of Advances in Modeling Earth Systems*, *6*, 223–248. doi: 10.1002/2013MS000282

Persson, P. O. G. (2002). Measurements near the atmospheric surface flux group tower at SHEBA: Near-surface conditions and surface energy budget. *Journal of Geophysical Research*, *107*. doi: 10.1029/2000JC000705

Pinto, J. O. (1998). Autumnal mixed-phase cloudy boundary layers in the Arctic. *Journal of the Atmospheric Sciences*, *55*(11), 2016–2038. Retrieved 2021-05-12, from `https://journals.ametsoc.org/view/journals/atsc/55/11/1520-0469_1998_055_2016_ampcbl_2.0.co_2.xml` (Publisher: American Meteorological Society Section: Journal of the Atmospheric Sciences) doi: 10.1175/1520-0469(1998)055⟨2016:AMPCBL⟩2.0.CO;2

Pithan, F., Ackerman, A., Angevine, W. M., Hartung, K., Ickes, L., Kelley, M.,

... Zadra, A. (2016). Select strengths and biases of models in representing the Arctic winter boundary layer over sea ice: the larcform 1 single column model intercomparison. *Journal of Advances in Modeling Earth Systems*. doi: 10.1002/2016MS000630

Pithan, F., Medeiros, B., & Mauritsen, T. (2014). Mixed-phase clouds cause climate model biases in Arctic wintertime temperature inversions. *Climate Dynamics*, *43*, 289–303. doi: 10.1007/s00382-013-1964-9

Pressel, K. G., Kaul, C. M., Schneider, T., Tan, Z., & Mishra, S. (2015). Large-eddy simulation in an anelastic framework with closed water and entropy balances. *Journal of Advances in Modeling Earth Systems*. doi: 10.1002/2015MS000496

Pressel, K. G., Mishra, S., Schneider, T., Kaul, C. M., & Tan, Z. (2017). Numerics and subgrid-scale modeling in large eddy simulations of stratocumulus clouds. *Journal of Advances in Modeling Earth Systems*. doi: 10.1002/2016MS000778

Randall, D. A., & Cripe, D. G. (1999). Alternative methods for specification of observed forcing in single-column models and cloud system models. *Journal of Geophysical Research*, *104*, 24527–24545. doi: 10.1029/1999JD900765

Savre, J., Ekman, A. M. L., Svensson, G., & Tjernstrm, M. (2015). Large-eddy simulations of an Arctic mixed-phase stratiform cloud observed during IS-DAC: sensitivity to moisture aloft, surface fluxes and large-scale forcing. *Quarterly Journal of the Royal Meteorological Society*, *141*, 1177–1190. doi: 10.1002/qj.2425

Schneider, T., Kaul, C. M., & Pressel, K. G. (2019). Possible climate transitions from breakup of stratocumulus decks under greenhouse warming. *Nature Geosci.*, *12*, 163–167.

Sekhon, R. S., & Srivastava, R. C. (1970). Snow Size Spectra and Radar Reflectivity. *Journal of the Atmospheric Sciences*, *27*, 299–307. doi: 10.1175/1520-0469(1970)027⟨0299:SSSARR⟩2.0.CO;2

Semtner, A. J. (1976). A Model for the Thermodynamic Growth of Sea Ice in Numerical Investigations of Climate. *Journal of Physical Oceanography*, *6*, 379–389. doi: 10.1175/1520-0485(1976)006⟨0379:AMFTTG⟩2.0.CO;2

Serreze, M. C., Barrett, A. P., Slater, A. G., Steele, M., Zhang, J., & Trenberth, K. E. (2007, June). The large-scale energy budget of the Arctic. *Journal of Geophysical Research*, *112*(D11). doi: 10.1029/2006JD008230

Shen, Z., Pressel, K. G., Tan, Z., & Schneider, T. (2020). Statistically steady state large-eddy simulations forced by an idealized GCM: 1. Forcing framework and simulation characteristics. *Journal of Advances in Modeling Earth Systems*, *12*. doi: 10.1029/2019MS001814

Shupe, M. D., & Intrieri, J. M. (2004). Cloud radiative forcing of the Arctic surface: The influence of cloud properties, surface albedo, and solar zenith angle. *Journal of Climate*, *17*, 616–628. doi: 10.1175/1520-0442(2004)017⟨0616:CRFOTA⟩2.0.CO;2

Stramler, K., Del Genio, A. D., & Rossow, W. B. (2011). Synoptically driven Arctic winter states. *Journal of Climate*, *24*(6), 1747–1762. Retrieved 2017-12-21, from http://journals.ametsoc.org/doi/abs/10.1175/2010JCLI3817.1 doi: 10.1175/2010JCLI3817.1

Tan, Z., Lachmy, O., & Shaw, T. A. (2019). The sensitivity of the jet stream response to climate change to radiative assumptions. *Journal of Advances in Modeling Earth Systems*, *11*(4), 934–956. doi: 10.1029/2018MS001492

Tan, Z., Schneider, T., Teixeira, J., & Pressel, K. G. (2016). Large-eddy simulation of subtropical cloud-topped boundary layers: 1. A forcing framework with closed surface energy balance. *Journal of Advances in Modeling Earth Systems*. doi: 10.1002/2016MS000655

Tan, Z., Schneider, T., Teixeira, J., & Pressel, K. G. (2017). Large-eddy simulation of subtropical cloud-topped boundary layers: 2. Cloud response to climate change. *Journal of Advances in Modeling Earth Systems*. doi:

10.1002/2016MS000804

Taylor, P. C., Boeke, R. C., Li, Y., & Thompson, D. W. J. (2019, July). Arctic cloud annual cycle biases in climate models. *Atmospheric Chemistry and Physics*, *19*(13), 8759–8782. doi: 10.5194/acp-19-8759-2019

Zhang, X., Schneider, T., & Kaul, C. M. (2020). Sensitivity of idealized mixed-phase stratocumulus to climate perturbations. *Quarterly Journal of the Royal Meteorological Society*, *146*(732). doi: 10.1002/qj.3846

Zhang, X., Schneider, T., Shen, Z., Pressel, K. G., & Eisenman, I. (2021a, December). *PyCLES with GCM forcing and simple sea ice.* Zenodo. Retrieved from `https://doi.org/10.5281/zenodo.5773210` doi: 10.5281/zenodo.5773210

Zhang, X., Schneider, T., Shen, Z., Pressel, K. G., & Eisenman, I. (2021b, December). *sally-xiyue/fms-idealized: FMS with thermodynamic sea ice.* Zenodo. Retrieved from `https://doi.org/10.5281/zenodo.5773236` doi: 10.5281/zenodo.5773236

Zuidema, P., & Joyce, R. (2008). Water vapor, cloud liquid water paths, and rain rates over northern high latitude open seas. *Journal of Geophysical Research: Atmospheres*, *113*(D5). doi: https://doi.org/10.1029/2007JD009040